J. Fluid Mech. (1996), vol. 310, pp. 215–241

Entrainment in a shear-free turbulent mixing layer

By D. A. BRIGGS,† J. H. FERZIGER, J. R. KOSEFF AND S. G. MONISMITH

Environmental Fluid Mechanics Laboratory, Department of Civil Engineering, Stanford University, Stanford, CA 94309-4020, USA

(Received 7 March 1995 and in revised form 23 October 1995)

Results from a direct numerical simulation of a shear-free turbulent mixing layer are presented. The mixing mechanisms associated with the turbulence are isolated. In the first set of simulations, the turbulent mixing layer decays as energy is exchanged between the layers. Energy spectra with $E(\kappa) \sim \kappa^2$ and $E(\kappa) \sim \kappa^4$ dependence at low wavenumber are used to initialize the flow to investigate the effect of initial conditions. The intermittency of the mixing layer is quantified by the skewness and kurtosis of the velocity fields: results compare well with the shearless mixing layer experiments of Veeravalli & Warhaft (1989). Eddies of size of the integral scale ($k^{3/2}/\epsilon$) penetrate the mixing layer intermittently, transporting energy and causing the layer to grow. The turbulence in the mixing layer can be characterized by eddies with relatively large vertical kinetic energy and vertical length scale. In the second set of simulations, a forced mixing layer is created by continuously supplying energy in a local region to maintain a stationary kinetic energy profile. Assuming the spatial decay of r.m.s. velocity is of the form $u \propto y^n$, predictions of common two-equation turbulence models yield values of n ranging from -1.25 to -2.5. An exponent of -1.35 is calculated from the forced mixing layer simulation. In comparison, oscillating grid experiments yield decay exponents between $n = -1$ (Hannoun *et al.* 1989) and $n = -1.5$ (Nokes 1988). Reynolds numbers of 40 and 58, based on Taylor microscale, are obtained in the decaying and forced simulations, respectively. Components of the turbulence models proposed by Mellor & Yamada (1986) and Hanjalić & Launder (1972) are analysed. Although the isotropic models underpredict the turbulence transport, more complicated anisotropic models do not represent a significant improvement. Models for the pressure–strain tensor, based on the anisotropy tensor, performed adequately.

1. Introduction

Turbulent mixing occurs in a wide variety of geophysical flows. For example, wind blowing over a lake or ocean generates a turbulent layer near the water surface which diffuses downward (Imberger & Patterson 1990). As a result, fluid from below is entrained by mechanisms such as engulfment and large-scale stirring produced by turbulence or instabilities. The effects of shear on the entrainment rate are important and have been studied widely for unstratified and stratified flows but will not be considered in this paper. The entrainment process is further complicated when a stable density gradient and rotation are included. Parameterization of the mixing

† Present address: Contra Costa Water District, PO Box H20, Concord, CA 94524, USA.

rate is necessary for the development of turbulence models which can be used in geophysical flow applications. However, as described in Fernando (1991), there is little consensus on the entrainment rate correlation and a more thorough study of the entrainment process is needed.

This paper describes the results of a set of turbulent mixing layer simulations that evolve without mean shear. In this flow the entrainment mechanisms associated with the turbulence may be isolated and the complications introduced by shear avoided. The mixing layer is the region between two homogeneous layers of differing kinetic energy. Two types of simulations are performed; in the first, the turbulence decays, while in the second, the region with higher kinetic energy is continuously forced to maintain a steady state. The simulation results are compared to experiments for validation and the turbulence structure is further investigated. The last two sections of the paper evaluate the accuracy of commonly used turbulence models. The effectiveness of individual model components as well as predictions of the spatial decay of kinetic energy are calculated. Correct prediction of the spatial decay is critical for an accurate formulation of the entrainment rate (Nokes 1988). The effects of stable stratification are currently being studied but will presented separately.

2. Mathematical details of the simulation

The three-dimensional pseudo-spectral code originally developed by Rogallo (1981) was used. The governing equations are transformed into Fourier space ($\kappa_1, \kappa_2, \kappa_3$) and advanced using a second-order Runge–Kutta method. Nonlinear terms are evaluated in physical space to save computation time. The solution consists of the Fourier coefficients representing the fluctuating velocity, $\hat{u}_i$, and fluctuating scalar, $\hat{\theta}$. The simulation is computed on an isotropic 128^3 grid (see Rogallo 1981 and Holt, Koseff & Ferziger 1992 for details).

2.1. *Initial conditions and forcing*

The initial flow field $\hat{\boldsymbol{u}}_o$ is created from a homogeneous, isotropic turbulent velocity field with a model energy spectrum (Lee & Reynolds 1985)

$$E(\kappa) \sim \begin{cases} \kappa^2, & \kappa < \kappa_p \\ \kappa^{-5/3}, & \kappa_p \leqslant \kappa \leqslant \kappa_c, \end{cases} \tag{2.1}$$

where κ_p is the peak wavenumber, equal to 8, and κ_c is the cut-off wavenumber, equal to 61. Chasnov (1994) showed that the model spectrum for low wavenumbers affects the decay rate of kinetic energy (and length-scale evolution). Therefore both $E(\kappa) \sim \kappa^2$ and $E(\kappa) \sim \kappa^4$ dependence for $\kappa < \kappa_p$ were studied. Multiplying $\hat{\boldsymbol{u}}_o$ by the desired spatial distribution $f(y)$ produces the inhomogeneous field $\hat{\boldsymbol{u}}$:

$$\hat{\boldsymbol{u}}(\kappa_x, y, \kappa_z) = f(y)\ \hat{\boldsymbol{u}}_o(\kappa_x, y, \kappa_z). \tag{2.2}$$

The result must then be projected onto a divergence-free field to enforce continuity. This operation does not affect the velocity by more than 3%. Periodic boundary conditions are imposed in all directions requiring that two mixing layers be included in the domain. For $f(y)$, a periodic array of Gaussians is used. For clarity, in the remainder of the paper the two mixing layers will be averaged and we shall discuss the result as if there were only a single mixing layer.

The decaying mixing layer evolves in the absence of turbulent production. In contrast, the forced mixing layer is sustained by continuously adding energy on the

high-energy side. This produces a flow analogous to an oscillating grid experiment. The energy is added locally by multiplying each component in the velocity field by a factor

$$\hat{u}_i(\kappa_x, y, \kappa_z) = \hat{u}_i(\kappa_x, y, \kappa_z)\,(1 + g(y)\; j(\kappa)), \tag{2.3}$$

where $g(y)$ and $j(\kappa)$ are functions used to localize the energy boosting in physical and wave space respectively, and $\kappa = (\kappa_x^2 + \kappa_z^2)^{1/2}$ is the radial wavenumber. The function $g(y) = C\,\exp\{-(y - y_s)^2\}$ restricts the energy addition to the centre of the computational domain, y_s, while $j(\kappa)$ is used to prevent energy addition at all wavenumbers.

The use of $j(\kappa)$ is essential for maintaining a stationary and well-resolved energy spectrum. Any energy added at the low wavenumbers will accumulate since little dissipation is occurring at these scales. At the highest wavenumbers, any energy addition goes directly into dissipation and tends to degrade the resolution of the calculation by increasing the kinetic energy in this part of the spectrum. Additionally, to emulate the effects of turbulence generated by an oscillating grid, the forcing should be restricted to a finite range of scales. For these reasons energy is not added to the extreme wavenumbers and $j(\kappa)$ is chosen as

$$j(\kappa) = \begin{cases} 1, & \kappa_l \leqslant \kappa \leqslant \kappa_h \\ 0, & \text{otherwise;} \end{cases} \tag{2.4}$$

where $\kappa_l = 3$ and $\kappa_h = 42$ are the lower and upper wavenumbers that are forced, respectively.

After 5 time steps the energy decays to about 95% of the original level and the amplitudes of the velocity coefficients are increased according to (2.3). The amplitude of C required to return the energy to the prescribed level is determined from the current energy in the flow. Approximately 1/3 of the required energy is added into each component ($\overline{u^2}$, $\overline{v^2}$, and $\overline{w^2}$). Among the components the amplitude of C is slightly and randomly re-scaled to ensure isotropic forcing. With the degree of randomness chosen the energy added to the components does not vary by more than 5% and on average, an equal amount of energy is added to $\overline{u^2}$, $\overline{v^2}$, and $\overline{w^2}$. After the velocity amplitudes are boosted according to (2.3), continuity is enforced by subtracting the divergent portion of the velocity field. This operation does not change the velocity field by more than 3%.

2.2. *Statistical methods*

Given that the turbulence is statistically homogeneous in the horizontal (x, z)-plane, the two-point velocity correlation tensor is

$$Q_{ij}(\boldsymbol{r}) = \overline{u_i(\boldsymbol{x})u_j(\boldsymbol{x} + \boldsymbol{r})}, \tag{2.5}$$

where $\boldsymbol{x}$ and $\boldsymbol{r}$ are the position and separation distance in the horizontal plane, respectively. The overbar denotes an ensemble average over the horizontal plane. The two-dimensional energy spectrum tensor, $E_{ij}(\boldsymbol{k})$, is related to $Q_{ij}(\boldsymbol{r})$ through an inverse Fourier transform

$$E_{ij}(\boldsymbol{k}) = \frac{1}{(2\pi)^2} \int Q_{ij}(\boldsymbol{r}) \mathrm{e}^{-\mathrm{i}\boldsymbol{k}\cdot\boldsymbol{r}} \mathrm{d}\boldsymbol{r} \tag{2.6}$$

where $\boldsymbol{k}$ is the two-dimensional wavenumber vector. The radial energy spectrum is formed by integrating $E_{ij}(\boldsymbol{k})$ over annuli in the (κ_x, κ_z) plane

$$E_{ij}(\kappa) = \int E_{ij}(\boldsymbol{k}) \mathrm{d}A(\boldsymbol{k}) \tag{2.7}$$

with $\kappa = |\boldsymbol{k}|$ defined as the magnitude of the wavenumber vector $\boldsymbol{k}$. This spectrum is used to study the dynamics of the mixing layer and to monitor the resolution of the calculation. Taking the one-dimensional transform of $Q_{ij}(\boldsymbol{r})$ when $\boldsymbol{r}$ is aligned with one of the horizontal directions ($\boldsymbol{r} = r\boldsymbol{e}_m$, for example) yields

$$E_{ij}(\kappa_m) = E_{ij}(\kappa \boldsymbol{e}_m) = \frac{1}{2\pi} \int_{-\infty}^{\infty} Q_{ij}(r\boldsymbol{e}_m) \mathrm{e}^{-\mathrm{i}\kappa r} \mathrm{d}r \tag{2.8}$$

where $E_{ij}(\kappa_m)$ is the one-dimensional energy spectrum and $\boldsymbol{e}_m$ is the unit vector in the m direction (Lee & Reynolds 1985).

We define the integral scale in the x-direction as

$$\Lambda_{ij,1} = \frac{1}{R_{ij}} \int_0^{\infty} Q_{ij}(r_1, 0) \mathrm{d}r_1 \tag{2.9}$$

where $R_{ij} = \overline{u_i(\boldsymbol{x}) u_j(\boldsymbol{x})} = Q_{ij}(0)$ is the Reynolds stress tensor. Using the Fourier transform relation (2.8), an alternative form of the above integral scale can be obtained

$$\Lambda_{ij,1} = \frac{\pi}{R_{ij}} E_{ij}(\kappa_1 = 0). \tag{2.10}$$

In general, the longitudinal integral scale is defined as

$$\Lambda_{11,1} = \frac{\pi}{R_{11}} E_{11}(\kappa_1 = 0) \tag{2.11}$$

and transverse integral length scales are defined as

$$\Lambda_{22,1} = \frac{\pi}{R_{22}} E_{22}(\kappa_1 = 0) \tag{2.12}$$

and

$$\Lambda_{33,1} = \frac{\pi}{R_{33}} E_{33}(\kappa_1 = 0). \tag{2.13}$$

Since the turbulence is axisymetric, the length scales for the z-direction, $\Lambda_{33,3}, \Lambda_{22,3}$, and $\Lambda_{11,3}$ are statistically identical to (2.11), (2.12), and (2.13) respectively, and are used for averaging purposes.

The Taylor microscales are defined as

$$\lambda_{ij,1} \equiv \frac{u_i'}{[\overline{(\partial u_j / \partial x_1)^2}]^{1/2}} \tag{2.14}$$

and are used to form a Reynolds number, $Re_\lambda = q\lambda_{11,1}/\nu$, where $q^2 = \overline{u_i u_i}$.

2.3. *Transport equations*

The transport equations for the Reynolds stresses are obtained by time averaging the fluctuating momentum equations and are written here for reference:

$$\frac{\partial}{\partial t}\overline{(u^2 + w^2)} = -\frac{\partial}{\partial y}\overline{(u^2 + w^2)v} + \frac{2}{\rho_o}\overline{p\left(\frac{\partial u}{\partial x} + \frac{\partial w}{\partial z}\right)} - 2\nu\left(\overline{\frac{\partial u}{\partial x_k}\frac{\partial u}{\partial x_k}} + \overline{\frac{\partial w}{\partial x_k}\frac{\partial w}{\partial x_k}}\right) + \nu\frac{\partial}{\partial y}\frac{\partial \overline{u^2}}{\partial y} + \nu\frac{\partial}{\partial y}\frac{\partial \overline{w^2}}{\partial y} + G_h(y), \tag{2.15}$$

$$\frac{\partial}{\partial t}\overline{v^2} = -\frac{\partial}{\partial y}\overline{v^3} + \frac{2}{\rho_o}\overline{p\frac{\partial v}{\partial y}} - \frac{2}{\rho_o}\frac{\partial}{\partial y}\overline{pv} - 2\nu\overline{\frac{\partial v}{\partial x_k}\frac{\partial v}{\partial x_k}} + \nu\frac{\partial}{\partial x_2}\frac{\partial \overline{v^2}}{\partial x_2} + G_v(y), \tag{2.16}$$

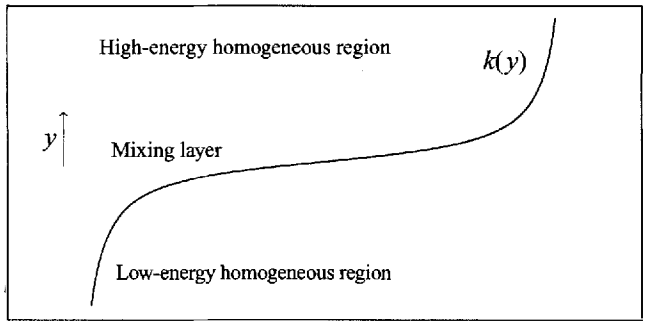

FIGURE 1. Initial kinetic energy profile for the decaying mixing layer.

$$\frac{\partial}{\partial t}(q^2/2) = -\frac{1}{2}\frac{\partial}{\partial y}\overline{(u^2+v^2+w^2)v} - \frac{1}{\rho_o}\frac{\partial}{\partial y}\overline{pv} - \nu\overline{\frac{\partial u_i}{\partial x_k}\frac{\partial u_i}{\partial x_k}} + \nu\frac{\partial}{\partial y}\frac{\partial(q^2/2)}{\partial y} + G_q(y), \tag{2.17}$$

where $G_h(y)$, $G_v(y)$, and $G_q(y)$ denote the contributions to the budgets from the source (these terms are zero for the decaying mixing layer). The scalar concentration is represented by θ and ρ_o is a reference density. The equations for the scalar variance

$$\frac{\partial}{\partial t}\overline{\theta^2} = -2\overline{v\theta}\frac{\partial \Theta}{\partial y} - \frac{\partial}{\partial y}\overline{v\theta^2} - 2\gamma\overline{\frac{\partial\theta}{\partial x_k}\frac{\partial\theta}{\partial x_k}} + \gamma\frac{\partial}{\partial y}\frac{\partial\overline{\theta^2}}{\partial y} \tag{2.18}$$

and turbulent scalar flux

$$\frac{\partial}{\partial t}\overline{v\theta} = -\frac{\partial}{\partial y}(\overline{v^2\theta}) - \overline{v^2}\frac{\partial\Theta}{\partial y} - \frac{1}{\rho_o}\frac{\partial}{\partial y}(\overline{p\theta}) + \overline{\frac{p}{\rho_o}\frac{\partial\theta}{\partial y}} + \frac{1+Pr}{Pr}\left\{\nu\frac{\partial^2}{\partial y^2}(\overline{v\theta}) - 2\nu\overline{\frac{\partial\theta}{\partial x_j}\frac{\partial v}{\partial x_j}}\right\} \tag{2.19}$$

are derived from the fluctuating v momentum and scalar concentration equations. Θ represents the mean scalar concentration at a given height.

3. Results

3.1. *Unforced mixing layer*

The decaying or unforced mixing layer consists of two regions of approximately homogeneous turbulence, with a kinetic energy ratio of about seven, separated by a smooth transition region (shown schematically in figure 1). As the kinetic energy decays the two regions also exchange energy. The mechanisms associated with entrainment, such as engulfment and turbulent diffusion, are isolated from the effects of mean shear and instabilities. This flow provides a basis for understanding the growth of a mixing layer due to the turbulent mechanisms alone.

The shearless mixing layer experiments of Veeravalli & Warhaft (1989) provide thorough documentation of the statistical quantities and serve as a standard of comparison. These experiments were performed in a wind tunnel with composite grids (or perforated plates) that generated two regions of turbulence, each with a different length scale. A short distance downstream of the grid each region developed

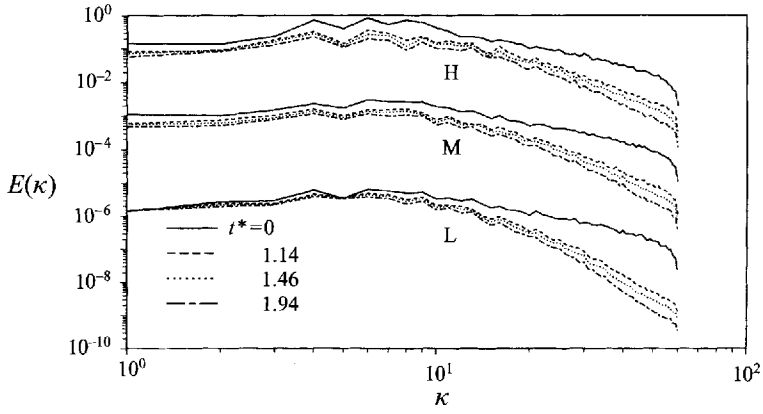

FIGURE 2. Evolution of radial energy spectra for the decaying mixing layer ($E(\kappa) \sim \kappa^2$) in the high (H) and low (L) energy homogeneous regions and mixing layer (M). The spectra for the mixing layer and low-energy region are offset by 10^{-2} and 10^{-4}, respectively.

a distinct kinetic energy. The two sides of the grid had equal solidity which allowed the flow to advect downstream with a uniform mean velocity (see Veeravalli & Warhaft (1989) for further details). The interaction between the two turbulent regions caused the mixing layer to grow with downstream distance. By contrast, in the simulation the kinetic energy decays and the mixing layer grows with time instead of distance downstream.

The initial parameters of the simulation were chosen to match the 3:1 perforated plate experiment of Veeravalli & Warhaft (1989) as closely as possible (3:1 denotes the ratio of the radii of the two sizes of holes in the plate). This particular experiment was chosen for its low microscale Reynolds number, although the Reynolds number in the simulation was still only about half as large. Unless specified otherwise, the results presented hereafter refer to the simulation with the $E(\kappa) \sim \kappa^2$ initial spectrum (this flow was chosen since the Reynolds number was slightly higher than for the $E(\kappa) \sim \kappa^4$ simulation). The relevant parameters of the initial flow fields are shown in table 1. As in the experiment, the simulated turbulent mixing layer is allowed to evolve for about 1 or 2 eddy turnover time scales, $\tau = k/\epsilon$, before it is considered truly turbulent. In figure 2 a time series of the radial energy spectrum $E(\kappa)$ for the decaying mixing layer simulation is shown for each of the homogeneous regions and the mixing layer. As the flow decays the small scales lose energy at a much faster rate than the large scales in all regions of the flow. This implies that the turbulence in the mixing layer becomes increasingly dominated by large scales as the flow evolves. The slope of the spectrum at low wavenumbers appears to be constant and is determined by the initial condition of $E(\kappa)$. These energy spectra also show that the flow is adequately resolved.

3.1.1. *Decay rates*

The decay rate of homogeneous grid turbulence has been thoroughly documented. Data from early experiments were well described by a power law (Batchelor 1953)

$$k/k_o = A(t/\tau)^n \tag{3.1}$$

where k_o is the initial kinetic energy, A is a constant, and time is made dimensionless by the initial eddy turnover time τ. Experiments (Gad-el-Hak & Corrsin 1974; Bradshaw 1975) suggest that n is in the range -1.1 to -1.7 with a consensus for a value near

	Decaying mixing layer	Veeravalli & Warhaft (1989)
$k_1 \equiv q_1^2/2\,(\mathrm{cm^2\,s^{-2}})$	0.55	81.5
$k_2 \equiv q_2^2/2\,(\mathrm{cm^2\,s^{-2}})$	4.14	510
$\epsilon_1\,(\mathrm{m^2\,s^{-3}})$	0.00017	0.090
$\epsilon_2\,(\mathrm{m^2\,s^{-3}})$	0.00225	0.655
$\lambda_1\,(\mathrm{cm})$	0.17	0.42
$\lambda_2\,(\mathrm{cm})$	0.14	0.37
$Re_{\lambda 1} \equiv \lambda_1 q_1/\nu$	17.8	33.5
$Re_{\lambda 2} \equiv \lambda_2 q_2/\nu$	40.3	73.9
$\tau_1 \equiv k_1/\epsilon_1\,(\mathrm{s})$	0.32	0.091
$\tau_2 \equiv k_2/\epsilon_2\,(\mathrm{s})$	0.18	0.078
Power law decay of kinetic energy $k/k_o \propto (t/\tau)^n$		
n_1, n_2	$-1.35, -1.55$	$-1.25, -1.43$

TABLE 1. Initial parameters of the simulation and experiments of Veeravalli & Warhaft (1989); the subscripts 1 and 2 refer to the low- and high-energy sides of the mixing layer, respectively. The experimental data refer to the 3:1 perforated plate configuration. For comparison purposes $\lambda = (\overline{u^2})^{1/2}/(\epsilon/15\nu)^{1/2}$ in this table only.

-1.2. Direct numerical simulation (DNS) of the decay of homogeneous turbulence performed by Riley, Metcalfe & Weissman (1981) indicate $n = -1.5$ for $Re_\lambda = 27.2$. Lee & Reynolds (1985) recorded power-law decay exponents of $n = -1.33$ to -1.67 for their DNS of decaying isotropic turbulence for $Re_\lambda = 20 - 60$ with $E(\kappa) \sim \kappa^2$ dependence for $\kappa \leqslant \kappa_p$. The large-eddy simulations of Chasnov (1994) exhibit decay exponents that approach $n = -1.2$ and -1.3 after a large number of eddy turnover times for $E(\kappa) \sim \kappa^2$ and κ^4 initial energy spectra, respectively. Decay rates in the current simulations are found to be $n = -1.55$ for the high-energy side and $n = -1.35$ for the low-energy side. The power-law exponents are obtained by fitting a line to the normalized kinetic energy (no virtual origin or offset is used) on a log-log plot. In general, exponents from direct numerical simulations are slightly higher than laboratory values. However, at lower Re the decay exponents are expected to be larger (Riley *et al.* 1981).

A simulation initiated with $E(\kappa) \sim \kappa^4$ dependence for $\kappa \leqslant \kappa_p$ was also completed to examine the effect of the initial energy spectra on decay rates and statistics. Both the κ^2 and κ^4 simulations were initiated with the same kinetic energy and Re. As shown in figure 3, the kinetic energy in the higher-energy region for both simulations decays at approximately the same rate but at a given time there is less energy in the κ^4 simulation. This is because the distribution of kinetic energy in the κ^4 simulation (more energy in the higher wavenumbers and less in the low wavenumbers) results in an initially higher dissipation. Subsequently, the energy in the flow became smaller than that derived from the κ^2 simulation. The power-law decay exponent for the κ^4 spectrum is $n = -1.6$, a slightly higher value compared to the κ^2 simulation. The effect of the initial spectrum on the statistics is discussed below.

3.1.2. *Turbulence statistics*

The moments of the turbulence were computed throughout the mixing layer. The only relevant time scales in the flow are those associated with the turbulence; therefore

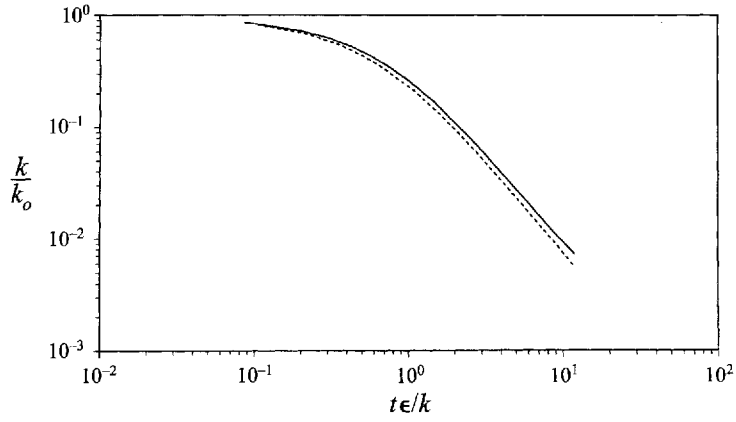

FIGURE 3. Temporal decay of kinetic energy for the $E(\kappa) \sim k^2$ (———) and $E(\kappa) \sim k^4$ (- - - -) simulations. The kinetic energy is normalized by the initial value.

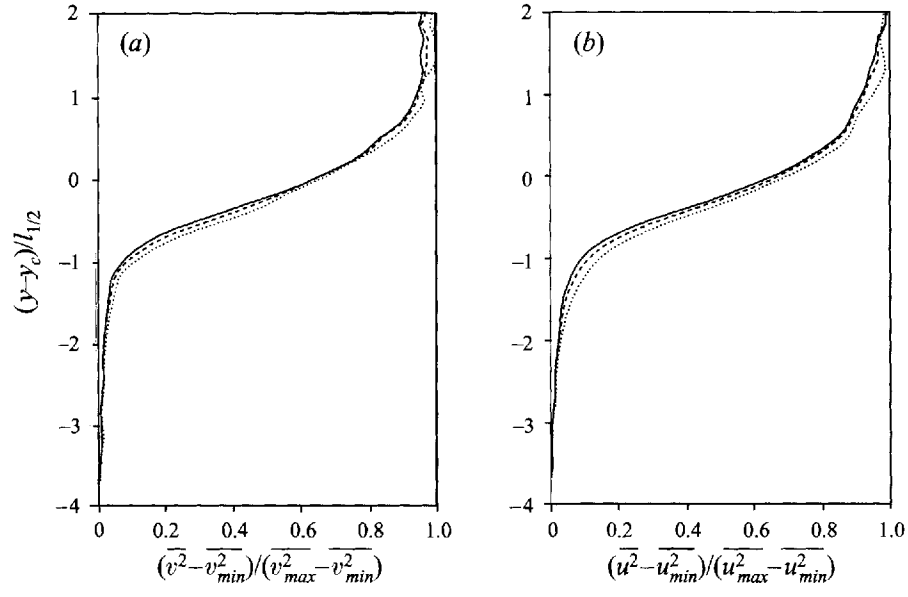

FIGURE 4. Variance of the vertical (*a*) and horizontal (*b*) velocity field for the decaying mixed layer. The curves represent the simulation values at $t^* = 0.875$ (———), $t^* = 1.16$ (- - - -) and $t^* = 1.72$ (·····). Time is normalized by the initial eddy turnover time.

time was non-dimensionalized with the initial eddy turnover time τ. Statistical moments for both mixing layers collapse to an asymptotic state (Veeravalli & Warhaft 1989) after one eddy turnover time. The variance profiles for $\overline{v^2}$ and $\overline{u^2}$, normalized to lie between 0 and 1, are shown in figure 4 at three different times. The location where the mapped variance is 0.5, defined as y_c, and the half-thickness, $l_{1/2}$, defined as the vertical distance between the locations with non-dimensionalized variance values 0.25 and 0.75, are used to centre and normalize the vertical coordinate. Even though the curves for $\overline{v^2}$ and $\overline{u^2}$ are similar, the large intermittent scales are slightly anisotropic in the mixing layer. This is discussed in more detail in §3.1.4.

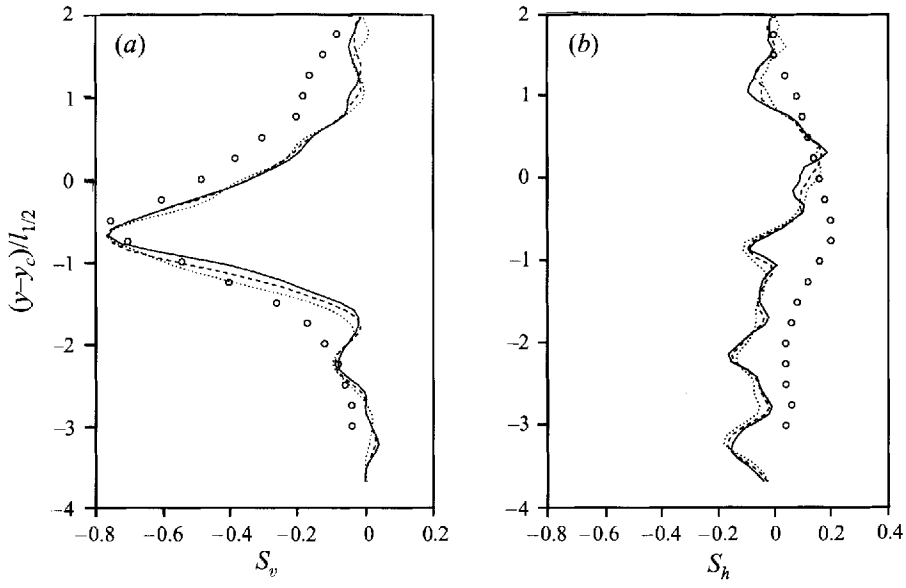

FIGURE 5. Normalized skewness of the vertical (*a*) and horizontal (*b*) velocity field for the decaying mixed layer. The curves represent the simulation values at $t^* = 0.875$ (———), $t^* = 1.16$ (– – – –) and $t^* = 1.72$ (·····). Data from Veeravalli & Warhaft (1989) (3:1 perforated plate) are also shown (○).

The skewness, $S \equiv \overline{u^3}/(\overline{u^2})^{3/2}$, of the velocity field is one indicator of intermittency. In figure 5(*a*) the normalized skewness of the vertical velocity, S_v, at three different times is shown together with averaged experimental results. The Gaussian value of zero is obtained in both homogeneous regions while, in the mixing layer, there is a significant negative deviation. This is attributed to large, intermittent structures penetrating downward from the high-energy region. Since the turbulence in the upper region is more energetic, the skewness is negative. The peak skewness occurs below the centre of the variance profile indicating the stronger influence of the high-energy region. The peak values of the skewness profile are nearly identical for the simulation and the perforated plate experiment and occur at approximately the same vertical location. The skewness of the horizontal velocity, S_h, should be zero. Figure 5(*b*) shows that although the skewness is non-zero, there is no perceivable trend. Averaging over a larger domain (or more realizations) would reduce S_h. A small but inexplicable peak is noticed in the experimental S_h.

As a further indication of the intermittency, the kurtosis, $K \equiv \overline{u^4}/(\overline{u^2})^2$, of the vertical and horizontal velocity fields, K_v and K_h, is calculated and shown in figure 6. Large values of the kurtosis are associated with a sample pool containing a small number of values far from the mean. Eddies with large vertical kinetic energy will appear intermittently in the mixing layer contributing to non-Gaussian values of the vertical kurtosis K_v. Similar trends in K_v are observed in both the experiment and simulation. Deviations of K_h from the homogeneous value occur because eddies that have large vertical kinetic energy will transport horizontal energy as they penetrate the mixing layer. Generally, the agreement between the simulations and experiments is good but the peak in the horizontal kurtosis K_h for the simulation is smaller. As the eddies penetrate the mixing layer and overturn, vertical energy may be transferred into horizontal components. However, less energetic eddies will decay before their energy can be transferred. Since the turbulence in the simulations is generally less

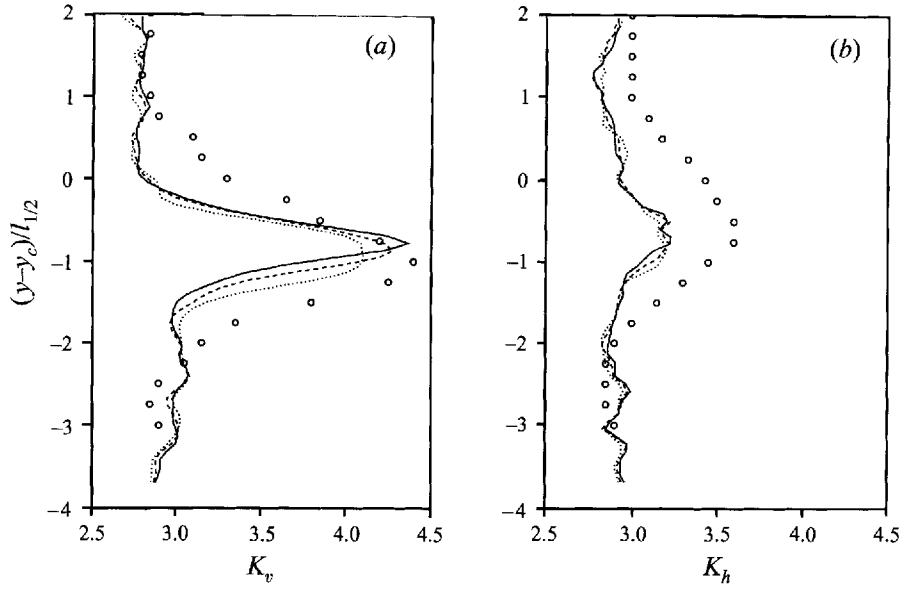

FIGURE 6. Normalized kurtosis of the vertical (*a*) and horizontal (*b*) velocity field for the decaying mixed layer. The curves represent the simulation values at $t^* = 0.875$ (———), $t^* = 1.16$ (– – – –) and $t^* = 1.72$ (·····). Data from Veeravalli & Warhaft (1989) (3:1 perforated plate) are also shown (○).

energetic compared to the experiments one might expect a smaller peak of K_h in the simulation. The location of the peaks in the kurtosis profiles, similar to those for the skewness, are located on the weaker side of the mixing layer, indicating the stronger influence of the higher-energy region. Outside the mixing layer, in the homogeneous regions, both K_v and K_h retain the Gaussian value of 3. Pope & Haworth (1987), using a p.d.f. model, also successfully reproduced the skewness and kurtosis observed in Veeravalli & Warhaft (1989).

The structure of the mixing layer is visualized with a planar view of contours of equal kinetic energy. In figure 7 a vertical plane at $t/\tau = t^* = 0.875$ is shown. The size of structures of high kinetic energy (which have closely spaced contour lines) is typically the integral scale; they are found throughout the mixing layer but less frequently on the weak side. In the low-energy region these structures are separated by areas with little or no energy and are responsible for the intermittency found in the statistics. The horizontal line in figure 7 marks the location in the mixing layer of the peak skewness. A model based on these observations is given in the Appendix.

3.1.3. *Effect of the energy initial spectrum and Reynolds number*

The profiles of the skewness and kurtosis for the $E(\kappa) \sim \kappa^4$ simulations are qualitatively similar to the $E(\kappa) \sim \kappa^2$ statistics discussed above, although the peaks are smaller. Since the κ^4 flow decays faster initially, has a smaller Re_λ (after a given t^*), and has less energetic large scales; the intermittent vertical scales in the mixing layer are less powerful and will produce smaller peaks in S and K.

The effect of the Reynolds number was evaluated by repeating the $E(\kappa) \sim k^2$ simulation at lower Re_λ ($Re_\lambda = 25$ as compared to $Re_\lambda = 40.3$) with the same initial conditions. The statistics of both simulations were compared after an equivalent dimensionless time. Generally, the peaks in the statistics for the lower Re_λ simulation were found to be smaller and closer to the high-energy side of the mixing layer. At

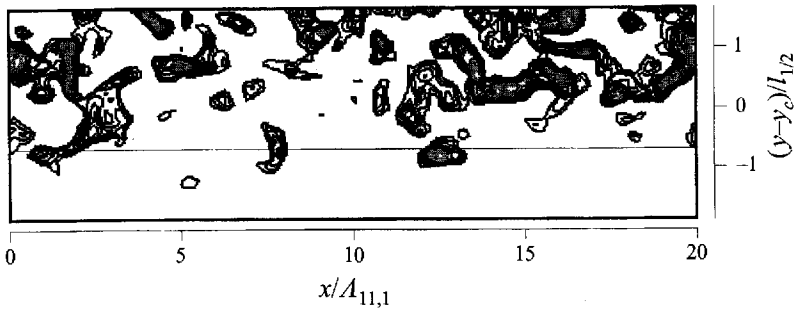

FIGURE 7. Kinetic energy contours for the decaying mixing layer in a vertical plane at $t^* = 0.875$. The horizontal line indicates the height of the peak skewness in the mixing layer. The horizontal axis is normalized by $\Lambda_{11,1}$ (evaluated in the high-energy homogeneous region).

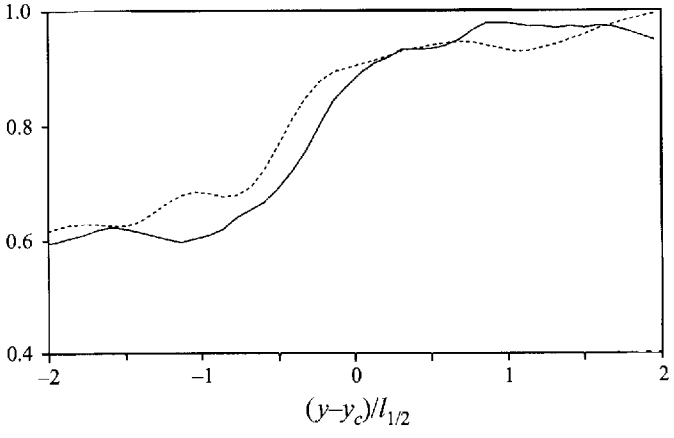

FIGURE 8. Profiles of the turbulent length scales across the mixing layer at $t^* = 0.875$: $l_v = (\overline{v^2})^{3/2}/\epsilon$ (– – – –), $l_u = (\overline{u^2})^{3/2}/\epsilon$ (———). Both length scales are normalized by l_o, the maximum value of l_v.

lower *Re*, diffusion contributes more to the growth of the mixing layer. Therefore, a less intermittent velocity field is expected.

3.1.4. *Length-scale distribution across the mixing layer*

The horizontal and vertical length scales associated with the largest eddies are defined as $l_u = (\overline{u^2})^{3/2}/\epsilon$ and $l_v = (\overline{v^2})^{3/2}/\epsilon$, respectively. These approximations to the integral length scales defined by (2.10) are used because the one-dimensional energy spectra are not smooth enough to discern the small changes in the integral length scale across the mixing layer, even after ensemble averaging over several flows. Profiles of l_v and l_u at $t^* = 0.875$ are shown in figure 8. In the homogeneous regions these scales are nearly equal, while in the mixing layer, l_v is larger than l_u. Eddies that penetrate the mixing layer from the high-energy region have most of their energy in the vertical component. Of these eddies, the ones that have the largest vertical scale (l_v) penetrate furthest into the mixing layer. As shown in figure 7, some of the largest turbulence eddies exist in the mixing layer, far from the high-energy region. Generally, turbulent eddies with $l_u > l_v$ have most of their energy in the horizontal components and do not travel far into the mixing layer. In the low-energy homogeneous region, beyond the reach of the largest intermittent scales, l_v and l_u become nearly equal again.

This length scale behaviour is similar to the results from VW. However, in the

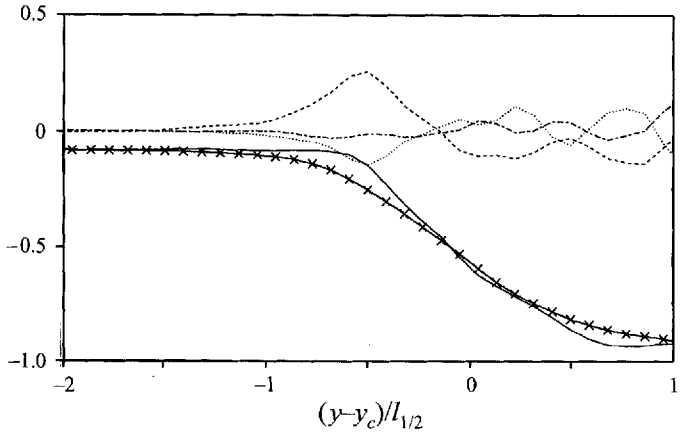

FIGURE 9. Terms in the decaying mixing layer budget equation for $\overline{v^2}$ (equation (2.16) with $G_y = 0$) at $t^* = 0.875$: $\partial\overline{v^2}/\partial t$ (———), dissipation (—⋆—), turbulent transport (– – – –), pressure transport (·····), pressure–strain (— — —). All terms are normalized by ϵ in the high-energy region. Diffusion is negligible and is not shown for clarity.

experiments, l_v exhibits a maximum in the mixing layer. As distance from the high-energy region increases, the large penetrating structures become more dominant as the local turbulence intensity decreases. This causes the vertical turbulent length scale to peak in the mixing layer. In comparison, the penetrating eddies in the simulation are less energetic and may not transport themselves as deeply into the mixing layer as the scales in the experiments. Consequently, the large intermittent scales in the mixing layer are not dominant enough to produce a peak in l_v.

The budget for the vertical component of the kinetic energy (equation (2.16) with $G_y = 0$) is shown in figure 9 at $t^* = 0.875$. This component is analysed because its transport is the largest, relative to $\overline{u^2}$ and $\overline{w^2}$, and the contributions from the pressure transport and pressure–strain terms are important. In the homogeneous regions the balance is primarily between dissipation and the time rate of change of $\overline{v^2}$. In the mixing layer, however, the transport contributes significantly to the budget. Transport of $\overline{v^2}$ by the turbulence, $-\partial\overline{v^3}/\partial y$, is large, due to the presence of the intermittent penetrating eddies emanating from the high-energy region, where the turbulence transport is negative. Since the mixing layer is only weakly anisotropic, redistribution of the velocity components by the pressure–strain term $\overline{(2p/\rho_o)\partial v/\partial y}$ is small and its contribution to the budget in the mixing layer is negligible.

The transport by the fluctuating pressure field, $-\partial\overline{pv}/\partial y$, acts in opposition to $\partial\overline{v^3}/\partial y$ in the mixing layer. The pressure transport is negative since $\overline{pv}$ becomes smaller in the mixing layer as y decreases (moving from the high- to low-energy regions). This correlation is strongly positive near the high-energy region due to the low-pressure wakes ($p < 0$) behind the eddies that penetrate from the high-energy region. As these eddies move downward the fluid in front of them is pushed ($p > 0$) horizontally as well as vertically. Therefore, the correlation between positive pressure fluctuations and v is weaker. Far from the high-energy region the correlation begins to decrease as the vertical bursts from the high-energy turbulence become less frequent. Figure 10 shows contours in a vertical plane of downward velocity $-v$ (*a*) and negative pressure fluctuations $-p$ (*b*) at $t^* = 0.875$. Large eddies penetrating into the mixing layer from the high-energy region are coincident with low-pressure regions. The

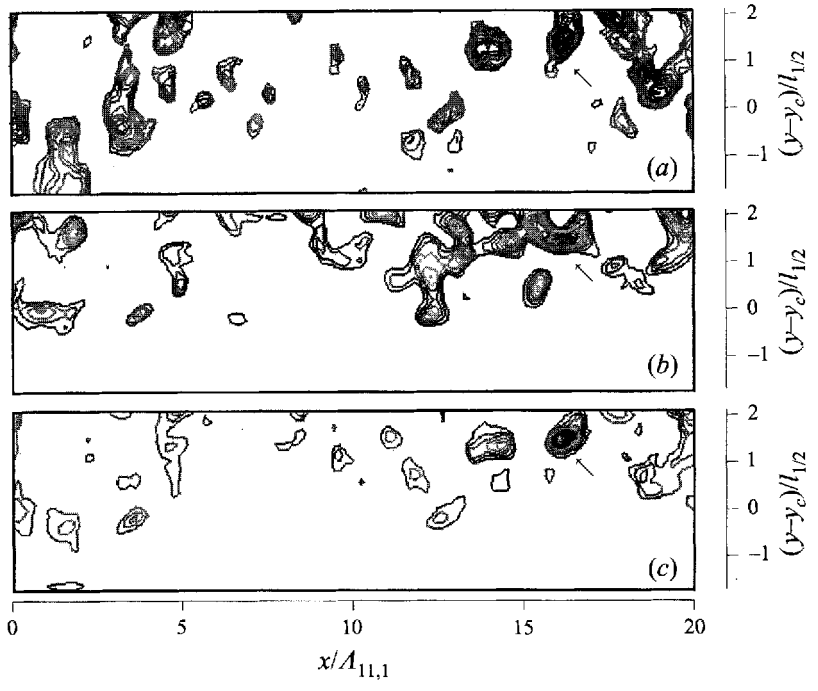

FIGURE 10. Contours in a vertical plane of fluctuating (*a*) $-v$, (*b*) $-p$, and (*c*) pv for the decaying mixing layer at $t^* = 0.875$. The arrow in (*a*) indicates a large downward-moving structure. A low pressure wake (fluctuating $p < 0$) follows the eddy, identified by the arrow in (*b*). The arrow in (*c*) indicates the resulting positive correlation between p and v. Several other examples can be found in the three planes. ($\Lambda_{11,1}$ is evaluated in the high-energy homogeneous region.)

contours in figure 10(*c*) show the resulting regions of positive correlation between p and v.

3.1.5. *Evolution of mean scalar field*

Initially, the mean scalar concentration, Θ, is different in the high- and low-energy homogeneous regions. The fluctuations of the scalar concentration, θ, are initially zero. The smooth interface that separates the two layers lies in the mixing layer between the two homogeneous regions. The evolution of Θ can also be used to quantify the intermittency of the mixing layer and transport mechanisms. Figure 11 shows the mean scalar field normalized between 0 and 1 for t^*=0, 0.51, and 1.16. The vertical coordinate is offset by y_Θ, the height where the normalized scalar value is 0.5, and normalized by the initial scalar half-width l_T, defined as the distance between the normalized scalar values of 0.25 and 0.75. In general there is a good collapse but the profile becomes asymmetric as time increases. The scalar field spreads faster on the high-energy side of the mixing layer compared to the weak side. This preferential spreading is caused by the large energetic structures that emanate from the high-energy region that transport fluid over a distance proportional to l_v. Since l_v is smaller than the interface thickness, these eddies do not affect the entire width of the scalar profile. On the weak side of the layer, the turbulence scales are smaller and weaker so the eddies are less effective at transporting the scalar (see figure 8). Figure 12 shows the time evolution of l_T, a measure of the thickness of the mixing layer, along with l_+, defined as the distance between the normalized scalar values of 0.25 and 0.5, and l_- defined as the distance between the normalized scalar values of

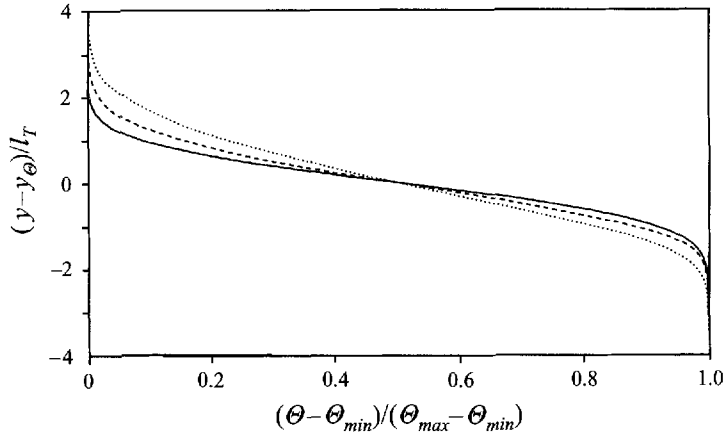

FIGURE 11. Evolution of normalized mean scalar profile. The curves represent the scalar at $t^* = 0$ (———), $t^* = 0.51$ (– – – –), $t^* = 1.16$ (·····). The vertical axis is normalized by the initial scalar half-width l_T at $t^* = 0$ and centred around the normalized scalar value of 0.5.

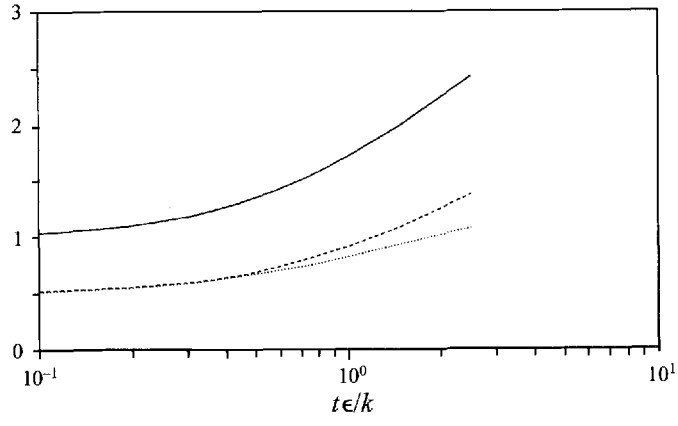

FIGURE 12. Evolution of scalar half-widths l_T (———), l_+ (– – – –), l_- (·····). All length scales are normalized by the initial value of l_T.

0.5 and 0.75. Although l_+ and l_- both contribute to the growth of the mixing layer, l_+ increases much faster than l_- causing the mean profile to develop asymmetrically. These results compare well with those of Jayesh & Warhaft (1994) in regions where stratification does not significantly affect the turbulence.

3.2. *Forced mixing layer*

The more geophysically relevant case of a forced mixing layer was also simulated. The energy profile is maintained by adding energy locally to the higher-energy side of the mixing layer. Turbulent entrainment develops as the turbulence diffuses from the source. Laboratory experiments use an oscillating grid to generate turbulence which then diffuses into the surrounding region (Hopfinger & Toly 1976; Hannoun, Fernando & List 1989). After about 5 eddy turnover times a steady kinetic energy profile developed in the simulation. The kinetic energy profiles before and after boosting are shown in figure 13. The passive scalar field, also shown in figure 13, was constructed with a sharp interface to simulate a thermocline. Relevant parameters at steady state for the homogeneous region above the mixing layer are displayed in

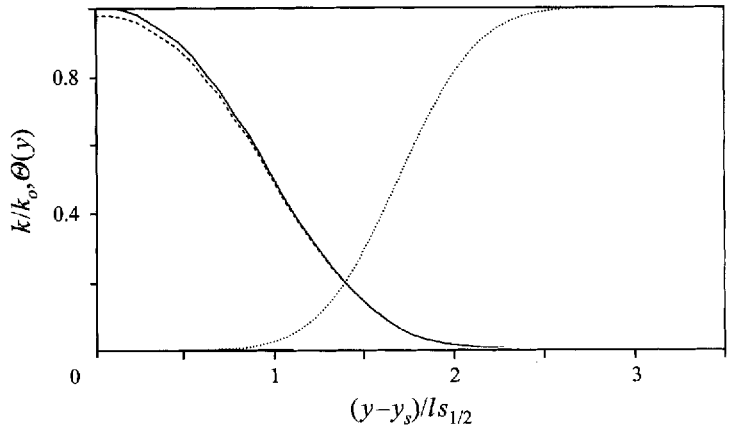

FIGURE 13. The normalized kinetic energy before (- - - -) and after (———) a boosting event displays the local influence of the source. k_o is evaluated at the centre of the source region after boosting. The distance from the centre of the source, $(y-y_s)$, is normalized by the source half-width, $ls_{1/2}$. The scalar profile is also sketched for reference (·····).

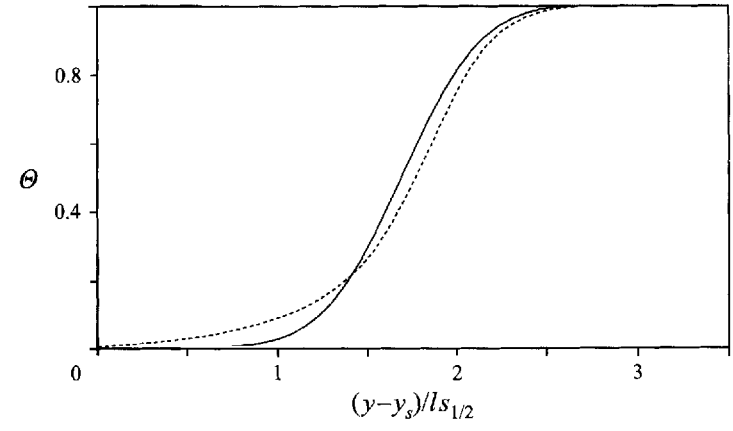

FIGURE 14. Propagation of the scalar interface: $t^* = 0$ (———), $t^* = 5.3$ (- - - -).

table 2. The horizontal coordinate represents distance from the source and is offset by the height of the centre of the source and normalized by the source half-width $ls_{1/2}$, defined as the height that contains 50% of the source energy. The interface is far enough from the source to ensure that the local turbulent kinetic energy is derived almost entirely from transport.

The scalar distribution at the beginning of the simulation and at $t^* = 5.3$ are shown in figure 14. Again, time is normalized by the initial eddy turnover time. The scalar profile does not remain symmetric. The large amount of kinetic energy above the interface increases the scalar concentration in this region as fluid of relatively high concentration below the interface is transported upwards by the turbulence. The interface propagates downward as the mixed layer grows. Far below the interface, the slow changes to the scalar field are caused mainly by molecular diffusion.

For numerical reasons the source cannot be restricted to a single horizontal plane. As discussed above, the source is represented by a narrow Gaussian function, $g(y)$. Continuity is enforced after each boosting event; this causes the source to be slightly less localized. Placement of the scalar interface is a compromise between minimizing

$k\,(\mathrm{cm}^2\,{}^{-2})$	7.5
$\epsilon\,(\mathrm{cm}^2\,\mathrm{s}^{-3})$	35
$\lambda\,(\mathrm{cm})$	0.15
$\Lambda\,(\mathrm{cm})$	0.21
Re_λ	58
$\tau = k/\epsilon\,(\mathrm{s})$	0.21

TABLE 2. Time-averaged quantities in the homogeneous region above the mixing layer

the effect of the source by placing the interface far away, and maintaining reasonably energetic turbulence in the mixing layer. At the location chosen, the transport of kinetic energy from the turbulence is approximately five times the contribution of the source. Below the interface the source is even less significant. This degree of influence of the source is deemed acceptable.

3.2.1. *Spatial dependence and isotropy*

When the flow reaches steady state, turbulent transport balances the dissipation far from the source and the kinetic energy profile becomes stationary. By contrast, the scalar field continues to evolve. The horizontal r.m.s. velocity, u', decays with distance from the source as $u' \propto (y_o/ls_{1/2})^n$ (shown in figure 15) where $n = -1.35$ and y_o is the distance from the centre of the source offset by the virtual origin. Using a method similar to Hannoun *et al.* (1989), the virtual origin is determined by extrapolating a line to the y-axis that is a best fit of $1/u'$ plotted *vs.* y' (y' an arbitrary distance from the grid). Only the mixing layer portion of the u' profile was fitted; it cannot be assumed that the power law applies throughout (an observation also made by Hopfinger & Toly 1976). The spatial decay rates in experiments range from $n = -1.0$ (Hannoun *et al.* 1989) to $n = -1.5$ (Nokes 1988). Many factors lead to the difference in decay exponents. In a thorough study of oscillating grid turbulence Nokes (1988) concluded that the exponent is dependent on the stroke and distance from the grid. Exponents ranging between -0.86 and -1.5 for the decay of r.m.s. horizontal velocities were recorded. De Silva & Fernando (1992) reported variations in the decay rate with grids of different solidity. Additionally, the decay exponent is sensitive to the choice of virtual origin. The spatial decay of kinetic energy was found to be proportional to $y_o^{-2.45}$ in the simulation. Laporta, Shao & Bertoglio (1995) developed a two-point model for inhomogeneous turbulence that yields a decay exponent of -3.

Further comparisons with laboratory oscillating grid experiments are made. The spatial dependence of the longitudinal integral length scale $\Lambda_{11,1}$ (2.11) and $Re_\Lambda = \Lambda_{11,1}q/\nu$ are shown in figure 16. As distance from the source increases $\Lambda_{11,1}$ grows linearly. The results are consistent with experiments which have shown $\Lambda \sim y$ (Hopfinger & Toly 1976 and Hannoun *et al.* 1988). Long (1978) states that the product of the integral length scale and turbulent velocity scale should be independent of distance from the turbulence source. Data from the experiments of Hopfinger & Toly (1976) show that Λu decays with distance from the source or remains constant, depending on the grid solidity and stroke. Simulated values of Re_Λ decrease with distance because q decays faster than Λ grows. One possible explanation for this dependence is the lower Reynolds number in the simulation ($Re_\Lambda = 58$) compared to

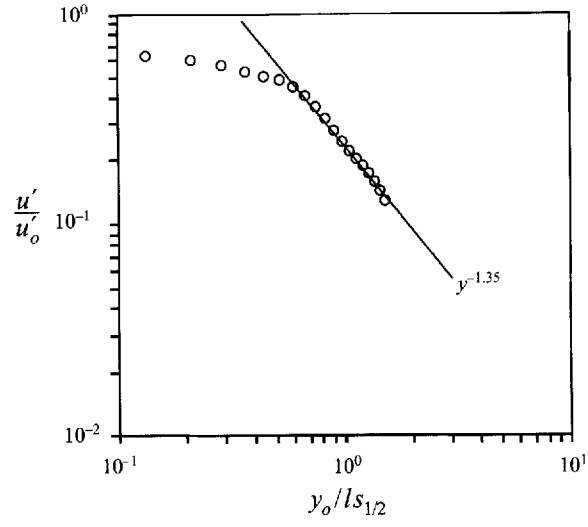

FIGURE 15. Decay of horizontal r.m.s. velocity with increasing distance from the source. The velocity is normalized by the value in the centre of the source region.

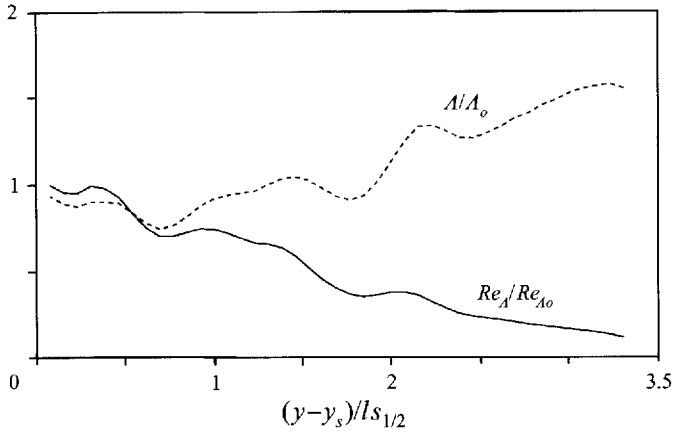

FIGURE 16. Spatial dependence of the integral length scale (- - - -) and $Re_\Lambda = \Lambda q/\nu$ (———). Both are normalized by their respective values at the centre of the source region.

laboratory experiments ($Re_\Lambda = 120$ for Hannoun *et al.* 1988 and $Re_\Lambda = 400-800$ for Hopfinger & Toly 1976, respectively).

In addition to Reynolds number effects, the spatial dependence of the integral scale may depend upon how the turbulence is produced. This can be explored using a simple theoretical model for the entrainment process which is outlined in the Appendix. It is shown that spatial variation of the length scale is dependent on the energy spectrum.

The method of energy addition renders the turbulence in the centre of the source region isotropic. As the kinetic energy front propagates outward the turbulence becomes anisotropic. After front propagation has ceased, v'/u' remains near 1.4 in the mixing layer (see figure 17). By contrast, vertically oscillating grid experiments produce extremely large v'/u' values near the source which then decrease with distance from the grid. Eddies that penetrate into the mixing layer contain relatively large

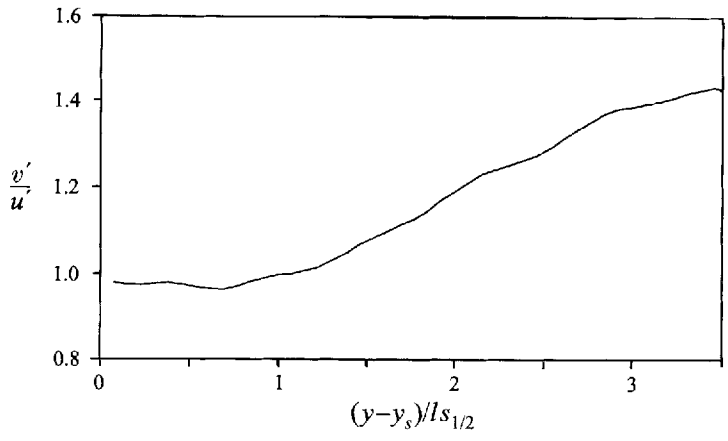

FIGURE 17. Anisotropy ratio v'/u'.

amounts of vertical kinetic energy. Therefore, the anisotropy ratio v'/u' is expected to be above unity in the mixing layer. In many experiments the ratio remains larger than 1 far from the grid (1.32 and 1.2 were reported by Hannoun *et al.* 1988 and Hopfinger & Toly 1976, respectively).

3.2.2. *The velocity field, turbulence structure, and kinetic energy budget*

The forced mixing layer is statistically stationary and averaging over time and horizontal planes gives smooth results. Compared to the decaying mixing layer, the intermittency is higher in the forced case, primarily because the kinetic energy ratio is larger and Re_λ is slightly higher. Near the source and below the mixing layer S_v and S_h are both nearly zero. Peak values of S_v and K_v reach -1.5 and 12, respectively, and are biased towards the weaker side of the mixing layer as in the decaying case.

The mechanisms of entrainment can be studied by examining planar views of the scalar concentration and kinetic energy. Numerous features are observed in the vertical plane shown in figure 18 (the vertical axis represents distance below the source). As in the decaying case, structures of the size of the integral scale deform the interface. These eddies intermittently penetrate deep into the low-turbulence region and mix fluids of different concentration (regions denoted by *a*). Fluid parcels are separated from other fluid of similar concentration (*b*) as a result of these large structures. Mixing occurs at small scales once the large scales have done the stirring (*c*). The interface is highly contorted on the high-energy side and relatively unperturbed on the opposite side. The interface thickness also varies with location and can be relatively thin (*d*). The large engulfing structures are apparent and coincide with mechanisms operating without the influence of buoyancy (Breidenthal 1992).

The terms in the kinetic energy balance (2.17) are averaged over time and are shown in figure 19. Beyond the region where the source dominates, the kinetic energy budget is a balance between transport and dissipation. The total transport of turbulent energy, the first two terms on the right-hand side of (2.17), is negative above the mixing layer and positive below it, indicating net transport of energy into the mixing layer. Diffusion of kinetic energy represents a small part of the budget.

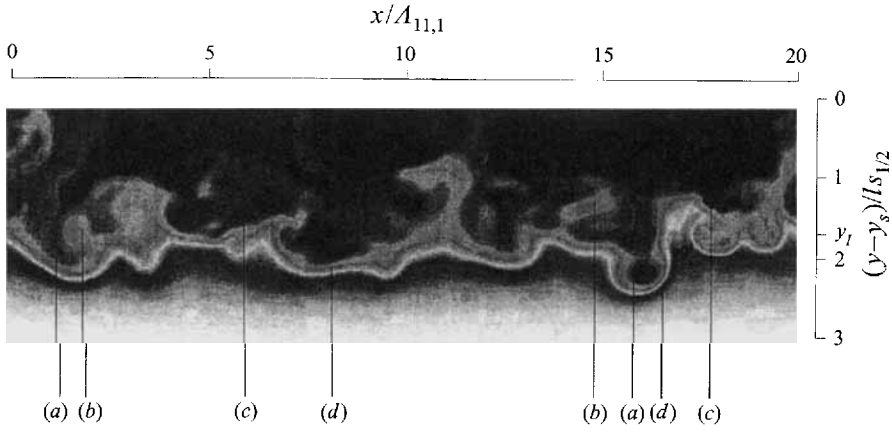

FIGURE 18. Scalar concentration in a vertical plane for the forced mixing layer. The following regions are marked: regions with large scales (*a*); regions where engulfment has pinched-off parcels of fluid of different concentration (*b*); regions marked by small-scale mixing (*c*); regions where the interface has become thin (*d*). The location of the mean interface height is denoted by y_I.

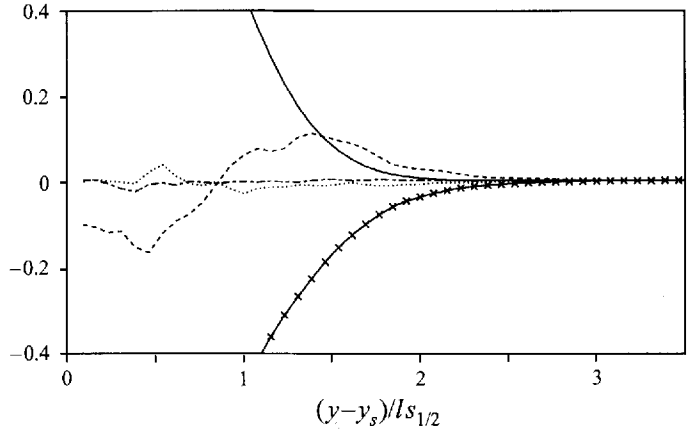

FIGURE 19. Transport terms in equation (2.17) for the forced mixing layer source (———), $\partial k/\partial t$ (·····), dissipation (—×—), turbulent and pressure transport (– – – –), diffusion of kinetic energy (— – —). All terms are normalized by the source value at $(y-y_s)/l_{1/2}=0$.

4. Turbulence models

A commonly used turbulence model for geophysical flows was developed by Mellor & Yamada (1986, referred to as MY below). Versions of this model include a complex, full Reynolds stress form and a simpler two-equation version similar to the model proposed by Launder (1990), the major difference being the determination of the length scale, l. A transport equation for l is used and the dissipation is parameterized in terms of k and l. The MY model uses assumptions first proposed by Rotta (1951) to model the turbulent transport. The constants in this model were evaluated using experimental data from homogeneous shear flows and regions of boundary layers where production is balanced by dissipation (buoyancy effects were absent). The model accurately reproduces flows used to calibrate it. However, in shearless mixing layers predictions may be inaccurate.

The correlation tensor

$$T_{ij2} = \overline{u_i u_j v} + \overline{pu_i}\delta_{j2} + \overline{pu_j}\delta_{i2} \tag{4.1}$$

is considered as a diffusive term (Hanjalić & Launder 1972, hereafter HL) and typically modelled as

$$T_{ij2} = -\frac{1}{\sigma_k}\frac{k}{\epsilon}\left(\overline{u_i v}\frac{\partial \overline{u_j v}}{\partial y} + \overline{u_j v}\frac{\partial \overline{u_i v}}{\partial y} + \overline{vv}\frac{\partial \overline{u_i u_j}}{\partial y}\right) \tag{4.2}$$

or in isotropic form

$$T_{ij2} = -\frac{2}{3\sigma_k}\frac{k^2}{\epsilon}\left\{\frac{\partial \overline{u_j v}}{\partial x_i} + \frac{\partial \overline{u_i v}}{\partial x_j} + \frac{\partial \overline{u_i u_j}}{\partial y}\right\} \tag{4.3}$$

while the MY model uses

$$T_{ij2} = \frac{3}{5}q^2 l S_q\left\{\frac{\partial \overline{u_j v}}{\partial x_i} + \frac{\partial \overline{u_i v}}{\partial x_j} + \frac{\partial \overline{u_i u_j}}{\partial y}\right\}, \tag{4.4}$$

where S_q and σ_k are model constants. We restrict our discussion to these components of the general tensor T_{ijk} since they correspond to transport in the one inhomogeneous direction. The correlations $T_{112} + T_{332}$, T_{222}, and T_{ii2} along with the isotropic HL (4.3) and MY (4.4) model predictions are shown in figure 20 using data from the forced mixing layer (the horizontal axis represents distance below the source). The length scale used in the MY model is the integral scale defined by (2.11). Near the source, at $(y - y_s) = 0$, the correlations and turbulence transport are approximately zero since the turbulence is homogeneous. In the mixing layer the turbulence is dominated by downward-moving intermittent structures which produce negative values of T_{222}, due primarily to large contributions from $\overline{vvv}$. The eddies that transport fluid from the source region carry both horizontal and vertical components of kinetic energy. This explains the large negative deviation of $T_{112} + T_{332}$ in the mixing layer. The isotropic models (4.3) and (4.4) underpredict the correlations, although the trends are correctly reproduced. Since the underprediction is not uniform among the components in the MY model, altering the model constants in (4.4) may not yield much improvement.

The predictions from the more complicated anisotropic model (4.2) are also shown in figure 20. In the anisotropic formulation more emphasis is placed on the vertical component of velocity. Owing to the anisotropy, this component makes the largest contribution to the transport in the mixing layer. As a result, the predictions are slightly better but are generally too small.

The MY models for $\overline{vv\theta}$ and $\overline{v\theta\theta}$ were also examined. These models are formulated similar to the transport correlations in (4.4) and are written as

$$\overline{vv\theta} = -2\, q^2 l\, S_{v\theta}\frac{\partial \overline{v\theta}}{\partial y} \tag{4.5}$$

and

$$\overline{v\theta\theta} = -q^2 l\, S_{\theta\theta}\frac{\partial \overline{\theta\theta}}{\partial y} \tag{4.6}$$

where $S_{\theta u}$ and $S_{\theta\theta}$ are model constants.

In figure 21(*a*) the profile of $\overline{vv\theta}$ is shown together with the predictions from the isotropic MY model (4.5) and an anisotropic model proposed by Craft, Graham &

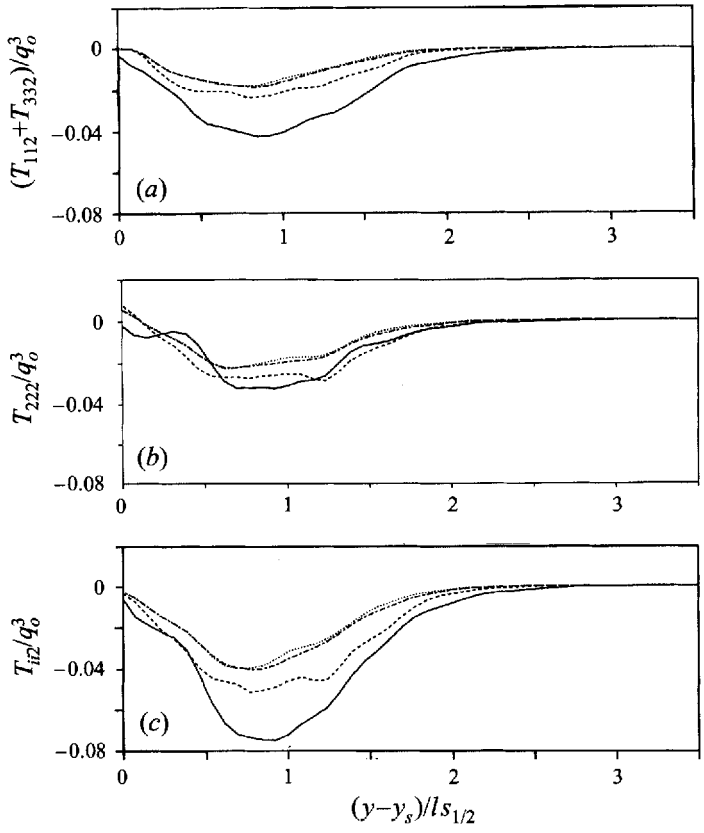

FIGURE 20. Profiles of the transport correlations (———), MY model (– – – –), HL isotropic model (·····), and HL anisotropic model (— – —). (*a*) $T_{112} + T_{332}$, (*b*) T_{222}, (*c*) T_{ii2}. Quantities are normalized by q^3 at $(y - y_s)/ls_{1/2}$=0. The horizontal axis represents distance below the source.

Launder (1993),

$$\overline{vv\theta} = -0.18\ \overline{vv}\ \frac{k}{\epsilon}\ \frac{\partial \overline{v\theta}}{\partial y}. \tag{4.7}$$

The correlation $\overline{vv\theta}$ is negative in the mixing layer because eddies with large vertical kinetic energy are correlated with negative θ-fluctuations. The predictions from the scalar flux models are poor because the parameterizations are inappropriate. In both formulations $\overline{vv\theta}$ is considered to be proportional to $\partial \overline{v\theta}/\partial y$. However, the profile of $\overline{v\theta}$ peaks in the mixing layer causing $\partial \overline{v\theta}/\partial y$ to change sign while $\overline{vv\theta}$ is consistently negative. The isotropic model (4.6), shown in figure 21(*b*), generally tracks $\overline{\theta\theta v}$ but is quantitatively incorrect.

The pressure–strain tensor, Π_{ij}, can be decomposed into slow and rapid contributions,

$$\Pi_{ij} = \Pi_{ij}^{(s)} + \Pi_{ij}^{(r)}. \tag{4.8}$$

Without mean shear, only the slow pressure–strain requires modeling. Typically, $\Pi_{ij}^{(s)}$ is assumed proportional to the anisotropy of the turbulence (Rotta 1951). Most models,

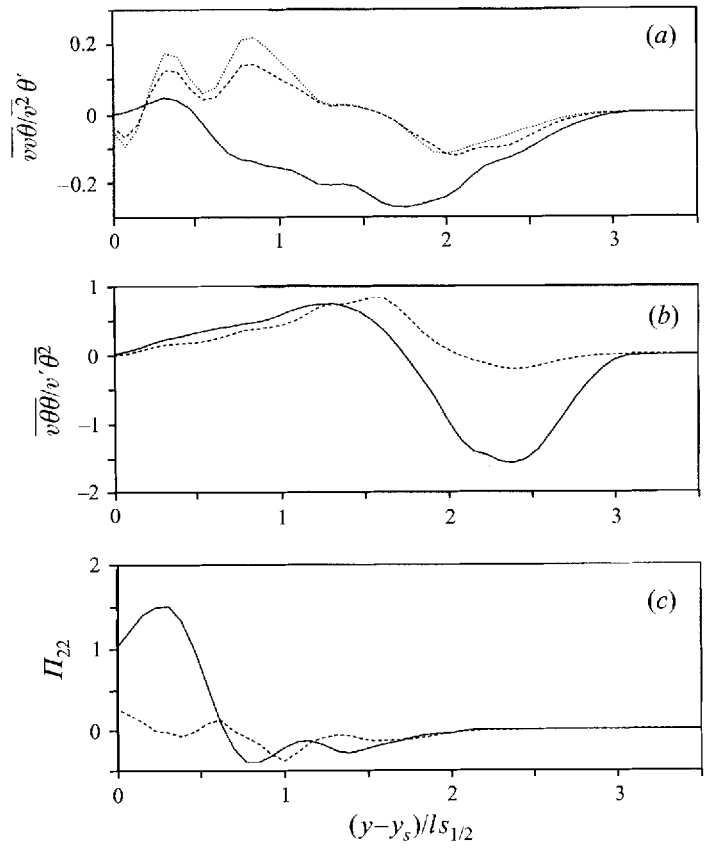

FIGURE 21. (*a*) Profile of $\overline{vv\theta}$ (———), MY model (– – – –), and anisotropic model of Craft *et al.*, (·····). The curves are normalized by $\overline{v^2}\theta'$, where θ' is an r.m.s. quantity, evaluated at $(y-y_s)/ls_{1/2}=0$. (*b*) Profile of $\overline{v\theta\theta}$ (———) and MY model (– – – –). The curves are normalized by $v'\overline{\theta^2}$, where v' is an r.m.s. quantity, evaluated at $(y-y_s)/ls_{1/2}=0$. (*c*) Profiles of Π_{22} (———) and predictions with MY model (– – – –). Quantities are normalized by Π_{22} at $(y-y_s)/ls_{1/2}=0$. The horizontal axes represent distance below the source.

including MY, represent the anisotropy to first order and model the pressure–strain as

$$\Pi_{ij} = -C_2\frac{q^3}{l}b_{ij}, \tag{4.9}$$

where $b_{ij} = \overline{u_iu_j}/q^2 - \delta_{ij}/3$. In the mixing layer, where $v'/u' > 1$, Π_{22} is negative because the pressure–strain term acts to return the turbulence to an isotropic state. As shown in figure 21(*c*) the MY model for Π_{22} generally yields the correct trend and is qualitatively correct in the mixing layer. In the source region, the agreement is poor. In the simulated flows described in this paper, the contribution of the pressure–strain tensor is much smaller than that of the transport terms. However, as *Re* increases, the pressure–strain terms should become more of a factor in the budget. Higher-*Re* simulations are needed to evaluate the model in a more challenging regime.

5. Predictions of kinetic energy spatial decay with models

The power-law dependence of the velocity field merits thorough examination because of its relation to the entrainment rate (Nokes 1988). When the mixing layer has

evolved to a state in which the transport balances the dissipation, the kinetic energy profile becomes stationary. Assuming a power-law dependence for all variables and a steady mixing layer, two-equation models yield a decay exponent with a given set of model constants. For the steady mixing layer the kinetic energy budget (2.17) simplifies to

$$\frac{\partial}{\partial y}\left(\frac{\overline{(u^2+v^2+w^2)v}}{2}+\frac{\overline{pv}}{\rho_o}\right)=-\epsilon. \tag{5.1}$$

Viscous diffusion of kinetic energy is disregarded since its contribution is approximately 5% of the budget. The source is also negligible in the mixing layer (see figure 19). Three two-equation models are examined. Each models the transport (the terms on the left-hand side of (5.1)) and the dissipation using a combination of two scalar variables: k and ϵ (Launder 1990), k and kl (MY) and k and ω (Wilcox 1988) where ω is an inverse time scale. The eddy viscosity is formed from the two variables to achieve closure. The three models are

$k-\epsilon$

$$\left.\begin{aligned}&\frac{\partial}{\partial y}\left(\frac{\nu_t}{\sigma_k}\frac{\partial k}{\partial y}\right)=\epsilon,\\&\frac{\partial}{\partial y}\left(\frac{\nu_t}{\sigma_\epsilon}\frac{\partial \epsilon}{\partial y}\right)=C_{\epsilon_2}\epsilon^2/k,\\&\nu_t=k^2/\epsilon,\ (\sigma_k,\sigma_\epsilon,C_\mu,C_{\epsilon_2})=(1,1.3,0.09,1.92);\end{aligned}\right\} \tag{5.2}$$

$k-kl$

$$\left.\begin{aligned}&\frac{\partial}{\partial y}\left(S_q\nu_t\frac{\partial q^2}{\partial y}\right)=2C_D q^3/l,\\&\frac{\partial}{\partial y}\left(S_l\nu_t\frac{\partial (q^2 l)}{\partial y}\right)=C_D q^3,\\&\nu_t=ql,\ (S_q,S_l,C_D)=(0.2,0.2,0.06),\quad q^2=2k;\end{aligned}\right\} \tag{5.3}$$

$k-\omega$

$$\left.\begin{aligned}&\frac{\partial}{\partial y}\left(C_{\mu_1}\nu_t\frac{\partial k}{\partial y}\right)=\beta_1 k\omega,\\&\frac{\partial}{\partial y}\left(C_{\mu_2}\nu_t\frac{\partial \omega}{\partial y}\right)=\beta_2\omega^2,\\&\nu_t=k/\omega,\ (\beta_1,\beta_2,C_{\mu_1},C_{\mu_2})=(3/40,9/100,0.5,0.5).\end{aligned}\right\} \tag{5.4}$$

Letting $k\sim Ky^\alpha$, $\epsilon\sim Ey^\beta$, $\omega\sim Wy^\delta$, $l\sim Ly^\sigma$ and $\nu_t\sim Vy^\gamma$ the exponents of spatial decay can be obtained analytically by substituting into (5.2)–(5.4). Each model yields a quadratic equation which produces two values of α. For each model it is possible to eliminate one root by physical arguments. In the case of the $k-\epsilon$ and $k-\omega$ models one of the roots is positive, which is impossible since energy must decay as distance increases from the source. For the $k-kl$ model both roots are negative but one of the roots results in an eddy viscosity that increases with distance from the source, making the eddy viscosity finite in regions in which the turbulence has not yet diffused. Table 3 shows the values of α based on the accepted values of the parameters for the two-equation models together with a summary of the simulation

	$k = Ky^{\alpha}$	$\nu_t = Vy^{\gamma}$	
	α	γ	
Two-equation models			
$k-\epsilon$	−4.9	−1.5	
$k-kl$	−2.8	−0.25	
$k-\omega$	−2.5	−0.43	
Simulation	−2.45	−0.42	($\nu_t = k^{1/2}l$)
Hopfinger & Toly (1976)	−2	0	($\nu_t = k^{1/2}l$)
Hannoun, Fernando & List (1988)	−1		(decay of r.m.s. u)
Nokes (1988)	−1 to −1.5		(decay of r.m.s. u)

TABLE 3. Power-law exponents for spatial dependence of k and ν_t

and experimental results. Experimental values for α range between −2 and −3 (Nokes 1988 reports a r.m.s. velocity decay as rapid as $y^{-1.5}$ which presumably corresponds to a kinetic energy decay law of about y^{-3}). Laboratory results indicate that the eddy viscosity, if modelled as $k^{1/2}l$ (Hopfinger & Toly 1976), is constant with distance since $k \sim y^{-2}$ and $l \sim y$. The predicted spatial dependence of the eddy viscosity for the models and simulation are also listed in table 3. All the two-equation models yield $l \sim y$, or $\sigma = 1$.

Compared to the experimental values, $\alpha \approx -2$ (Hopfinger & Toly 1975), and the simulation value of −2.45, the $k-\epsilon$ model value is too large. It can be expected that this large value of decay exponent will result in a slowly propagating interface. Both the $k-kl$ and $k-\omega$ models are better at reproducing experimental values of the spatial dependence of the kinetic energy and eddy viscosity. The model constants can be adjusted to yield the expected decay rates. For example, changing C_{ϵ_2} in the $k-\epsilon$ model from 1.92 to 2.5 will result in a decay exponent of $\alpha = -2.0$ but this may cause the model to predict other flows poorly.

6. Conclusions

A simulation of a decaying, shear-free mixing layer compares well with the experiments of Veeravalli & Warhaft (1989). In particular, the intermittency of the mixing layer, quantified by the skewness and kurtosis, is in excellent agreement. The temporal decay of kinetic energy in the decaying mixing layer compares well with other simulations and experiments. The simulations that were initialized with $E(\kappa) \sim \kappa^4$ dependence at low wavenumber were found to decay faster initially than the $E(\kappa) \sim \kappa^2$ flow. After 2 eddy turnover time scales, however, the two simulations exhibited similar power-law decay exponents. The turbulent eddies in the mixing layer that produce the intermittency and transport are characterized by relatively large vertical kinetic energy and large vertical length scale. Low-pressure wakes are created behind eddies as they penetrate the mixing layer. The pressure field removes energy from these eddies and produces negative pressure transport in the mixing layer.

For the forced mixing layer simulations, the spatial dependence of the kinetic energy and integral length scale are similar to those observed in oscillating grid experiments. The anisotropy ratio, v'/u', remains larger than unity in the mixing layer.

Isotropic models (Mellor & Yamada 1986; Hanjalić & Launder 1972) generally underpredict the transport correlations. The underprediction is fairly uniform for the Hanjalić & Launder (1972) model which suggests that an alteration of the con-

stants will improve the accuracy. An anisotropic model, although more complicated, performs slightly better. This improvement is due to the emphasis on the vertical component of velocity. A common model of the pressure–strain tensor was found to be generally accurate.

The spatial decay rate predicted by the $k-\epsilon$ model is approximately twice the value recorded in experiments. Predictions with the $k-kl$ and $k-\omega$ models are within an acceptable range. The decay exponent calculated from the simulation is also near experimental values.

Future simulations will include the effects of a stable density gradient. Increasing Re_λ will also be attempted.

We thank the reviewers for their comments and suggestions. The authors also wish to thank the Office of Naval Research for support of this work through grant number N00014-92-J-1611, monitored by Dr L. Goodman. Mr M. Stacey and Dr C. Rehmann helped develop some of the concepts through many useful discussions.

Appendix. 'Kinetic theory' model of entrainment

The contours of kinetic energy in the figures suggest that the mechanism of entrainment in shear-free mixing layers involves the creation of relatively large energetic eddies in the source region and the subsequent motion of these eddies into the low-energy region. This suggests the following model for the process.

Imagine that an eddy of diameter ℓ and speed v is injected into the flow in the source region. Assume that the size of the eddy remains unchanged as it moves but its speed is reduced by drag. We picture this eddy as something like a hard sphere, which is why we call this a kinetic theory model.

The equation of motion for such an eddy is

$$\frac{4\pi}{3}\ell^3\rho\frac{\mathrm{d}v}{\mathrm{d}t} = -\pi\ell^2 C_D\frac{\rho v^2}{2} \tag{A 1}$$

where C_D is the drag coefficient. At the low Reynolds numbers of interest here, it is reasonable to assume that $C_D \approx 24Re^{-1}$ where $Re = v\ell/\nu$ (White 1973); deviations from this approximation will be discussed below.

Since time does not appear explicitly in (A 1), we may consider v to be a function of the distance along the trajectory s and write

$$\frac{\mathrm{d}v}{\mathrm{d}t} = \frac{\mathrm{d}v}{\mathrm{d}s}\frac{\mathrm{d}s}{\mathrm{d}t} = v\frac{\mathrm{d}v}{\mathrm{d}s}. \tag{A 2}$$

With the aid of (A 2), (A 1) reduces to

$$\frac{\mathrm{d}v}{\mathrm{d}s} = -9\frac{\nu}{\ell^2} \tag{A 3}$$

which is easily integrated to give

$$\frac{v}{v_0} = \left(1 - 9\frac{\nu}{v_0\ell^2}s\right). \tag{A 4}$$

This result holds only when $v > 0$, i.e. when $s < v_0\ell^2/9\nu$.

To simplify matters, the source is idealized as a plane. To calculate the energy as a function of the distance from this plane, one must take into account that eddies of various sizes are produced and determine which eddies make the greatest contribution

to the energy at a given z. One might surmise that, at large distances from the source, the largest eddies are most important and assume that the distribution or spectrum (expressed in terms of length scale) has the form

$$E(\ell) = A\,\ell^{-r} \tag{A 5}$$

for large ℓ. This is equivalent to a spectrum in terms of wavenumber which behaves as k^{r-2} for small k, which suggests that reasonable values of r might lie in the range 4–6.

Equation (A 4) shows that the penetration depth of an eddy of size ℓ is $v_0(\ell)\ell^2/(9\nu)$. The characteristic velocity of an eddy with size ℓ given the spectrum (A 5) is $v_0(\ell) = A^{1/2}\ell^{(-r+1)/2}$. For $r = 4$, this gives a penetration depth which increases as $\ell^{1/2}$ for large ℓ. On the other hand, for $r = 6$, the penetration depth decreases as $\ell^{-1/2}$ for large ℓ. Thus, for $r = 4$, the largest eddies dominate at large distances, while for $r = 6$, eddies at the peak of the spectrum are likely to be more important. The former case should give a length scale which increases with distance from the source while the latter should give a constant length scale. Note that the dependence of the penetration depth on ℓ is weak and, as these results are based on an oversimplified model, they must be regarded with suspicion. On the other hand, the sensitivity of the behaviour of the turbulence energy to details of the source was observed in the simulations and is therefore likely to be correct. In particular, the length scale may not always increase linearly with depth as many people assume and most models predict.

This model also predicts that the anisotropy increases with distance from the source. It is difficult to determine whether this is supported by the simulations because the decay is too rapid to allow an accurate assessment to be made. The model is even simpler if it is assumed that the drag coefficient is independent of Reynolds number. This should be true at high Re but it is unlikely to be valid under the conditions of the experiments and the simulations reported herein.

The fact that this simple model predicts many of the experimental and simulation results lends support to the proposed mechanism of entrainment.

REFERENCES

Batchelor, G. K. 1953 *The Theory of Homogeneous Turbulence*. Cambridge University Press.

Bradshaw, P. 1975 *An Introduction to Turbulence and its Measurement*. Pergamon.

Breidenthal, R. E. 1992 Entrainment at thin stratified interfaces: The effects of Schmidt, Richardson, and Reynolds number. *Phys. Fluids* A **4**, 2141–2144.

Chasnov, J. R. 1994 Similarity states of passive scalar transport in isotropic turbulence. *Phys. Fluids* **6**, 1036–1051.

Craft, T. J., Graham, L. J. W. & Launder, B. E. 1993 Impinging jet studies for turbulent model assessment–II. An examination of the performance of four turbulent models. *Intl J. Heat Mass Transfer* **36**, 2685–2697.

De Silva, I. P. D. & Fernando, H. J. S. 1992 Some aspects of mixing in a stratified turbulent patch. *J. Fluid Mech.* **240**, 601–625.

Fernando, H. J. S. 1991 Turbulent mixing in stratified fluids. *Ann. Rev. Fluid Mech.* **23**, 455–93.

Gad el Hak, M. & Corrsin, S. 1974 Measurements of the nearly isotropic turbulence behind a uniform jet grid. *J. Fluid Mech.* **62**, 115–143.

Hanjalić, K. & Launder, B. E. 1972 A Reynolds stress model of turbulence and its application to thin shear flows. *J. Fluid Mech.* **52**, 609–638 (referred to herein as HL).

Hannoun, I. A., Fernando, H. J. S. & List, E. J. 1989 Turbulence structure near a sharp density interface. *J. Fluid Mech.* **180**, 189–209.

Holt, S. E., Koseff, J. R. & Ferziger, J. H. 1992 A numerical study of the evolution and structure of homogeneous stably stratified sheared turbulence. *J. Fluid Mech.* **237**, 499–539.

HOPFINGER, E. J. & TOLY, J.-A. 1976 Spatially decaying turbulence and its relation to mixing across density interfaces. *J. Fluid Mech.* **78**, 155–175.

IMBERGER, J. & PATTERSON, J. C. 1990 Physical limnology. In *Advances in Applied Mechanics*, pp. 303–475. Academic.

JAYESH & WARHAFT, Z. 1994 Turbulent penetration of a thermally stratified interfacial layer in a wind tunnel. *J. Fluid Mech.* **277**, 23–54.

LAPORTA, A., SHAO, L. & BERTOGLIO, J. P 1995 A two-point model for inhomogeneous turbulence and comparisons with large-eddy simulation. Abstract submitted to the *Tenth Symposium on Turbulent Shear Flows, Penn State, 1995.*

LAUNDER, B. E. 1990 A preview of turbulence modelling at UMIST. Presented at *UMIST 4th Biennial Colloquium on Computational Fluid Dynamics, Manchester Univ., 1990.*

LEE, M. J. & REYNOLDS, W. C. 1985 Numerical experiments on the structure of homogeneous turbulence. *Rep.* TF-24. Mechanical Engineering Dept., Stanford University.

LONG, R. R. 1978 A theory of mixing in a stably stratified fluid. *J. Fluid Mech.* **84**, 113–124.

MELLOR, G. L. & YAMADA, T. 1986 Development of a turbulence closure model for geophysical fluid problems. *Rev. Geophys. Space Phys.* **20**, 851–875 (referred to herein as MY).

NOKES, R. I. 1988 On the entrainment across a density interface. *J. Fluid Mech.* **188**, 185–204.

POPE, S. B. & HAWORTH, D. C. 1987 The mixing layer between turbulent fields of different scale. In *Turbulent Shear Flows 5* (ed. L. T. S. Bradbury *et al.*), pp. 44–53. Springer.

RILEY, J. J., METCALFE, R. W. & WEISSMAN, M. A. 1981 Direct numerical simulations of homogeneous turbulence in density stratified fluids. In *Non-linear Properties of Internal Waves* (ed. B. J. West), AIP Conf. Proc. Vol 76, pp. 78–110.

ROGALLO, R. S. 1981 Numerical experiments in homogeneous turbulence. *NASA Tech. Mem.* 81835.

ROTTA, J. C. 1951 Statistische Theorie nichthomogener Turbulenz. *Z. Phys.* **129**, 547–572.

VEERAVALLI, S. & WARHAFT, Z. 1989 The shearless turbulence mixing layer. *J. Fluid Mech.* **207**, 191–229.

WHITE, F.M. 1974 *Viscous Fluid Flow*. McGraw-Hill.

WILCOX, D. C. 1988 Reassessment of the scale-determining equation for advanced turbulence models. *AIAA J.* **26**, 1299–1310.